

Central discontinuous Galerkin methods for ideal MHD equations with the exactly divergence-free magnetic field

Fengyan Li^{*}, Liwei Xu, Sergey Yakovlev

Department of Mathematical Sciences, Rensselaer Polytechnic Institute, Troy, NY 12180-3590, United States

ARTICLE INFO

Article history:

Received 25 October 2010

Received in revised form 25 February 2011

Accepted 3 March 2011

Available online 14 March 2011

Keywords:

Ideal magnetohydrodynamic (MHD) equations

Divergence-free magnetic field

Central discontinuous Galerkin methods

High order accuracy

Overlapping meshes

ABSTRACT

In this paper, central discontinuous Galerkin methods are developed for solving ideal magnetohydrodynamic (MHD) equations. The methods are based on the original central discontinuous Galerkin methods designed for hyperbolic conservation laws on overlapping meshes, and use different discretization for magnetic induction equations. The resulting schemes carry many features of standard central discontinuous Galerkin methods such as high order accuracy and being free of exact or approximate Riemann solvers. And more importantly, the numerical magnetic field is exactly divergence-free. Such property, desired in reliable simulations of MHD equations, is achieved by first approximating the normal component of the magnetic field through discretizing induction equations on the mesh skeleton, namely, the element interfaces. And then it is followed by an element-by-element divergence-free reconstruction with the matching accuracy. Numerical examples are presented to demonstrate the high order accuracy and the robustness of the schemes.

© 2011 Elsevier Inc. All rights reserved.

1. Introduction

Many interesting problems in astrophysics, space physics and engineering can be described by magnetohydrodynamic (MHD) equations, and therefore it is of great importance to design accurate and robust numerical methods for such equations. In this paper, we focus on the reliable high order numerical methods for ideal MHD equations when relativistic, viscous, and resistive effects can be neglected, and these equations consist of a set of nonlinear hyperbolic conservation laws.

Besides the standard difficulty in solving nonlinear hyperbolic equations [20], one complexity in simulating the MHD system is associated with the interrelation of the performance of schemes and the numerical divergence of the magnetic field. Though the divergence of the exact magnetic field is always zero when it is zero initially, numerical evidence and some analysis indicate that the nonzero divergence of the computed magnetic field can be responsible for numerical instability or nonphysical features in approximated solutions [18,7,5,31,21,6]. This has been driving the development of various divergence-cleaning or divergence-free numerical algorithms for MHD equations, see e.g. [7,16,5,31,15,21,17,23,4] and the references therein. This also motivates the present work.

In this paper, central discontinuous Galerkin (DG) methods are developed for two-dimensional ideal MHD equations. There is no essential difficulty to extend the methods to three dimensions, but we will not consider it in this paper. Our methods are based on the central DG methods of Liu et al. [26,27] designed for hyperbolic conservation laws on overlapping meshes, with different discretization for magnetic induction equations. More specifically, while other conservative quantities are evolved with the central DG methods of [26], the magnetic field (or its two components in two dimensions) is

^{*} Corresponding author.

E-mail addresses: lif@rpi.edu (F. Li), xul3@rpi.edu (L. Xu), yakovs@rpi.edu (S. Yakovlev).

updated in such a way that its normal component is first approximated by discretizing magnetic induction equations on the mesh skeleton, namely, the element interfaces, and then an element-by-element divergence-free reconstruction procedure with matching accuracy will follow. This will lead to an exactly divergence-free magnetic field approximation provided that the electric field flux, used to discretize induction equations, is single-valued at grid-points. Fortunately this property is provided naturally by the present framework. The resulting methods (i) are high order accurate and (ii) free of exact or approximate Riemann solvers which can be complicated for the MHD system (e.g. [28,13,22]); (iii) provide magnetic field approximations with the exact zero divergence, instead of zero divergence in some discretized form or up to certain order of accuracy; (iv) need no reconstruction from the cell average of solutions over certain stencil to achieve high order accuracy due to their finite element nature; (v) need no averaging or interpolation step to have the single-valued electric field flux at grid-points. One factor which contributes to some of the above features is the extra information provided by the two copies of numerical solutions of the proposed methods defined on overlapping meshes.

Our work is related to the constraint transport methodology (see, e.g. [16,5,17,23]) which uses the magnetic flux as a fundamental variable and works with the induction equation system in its integral form. It is also a continuation of the earlier exploration by one of the authors to handle the divergence-free condition in the context of the DG framework in [10,21], where locally divergence-free DG methods were introduced for Maxwell equations and ideal MHD equations, with the use of piecewise divergence-free polynomials as the discrete space for the magnetic field. The methods demonstrated enhanced stability and accuracy in some examples for ideal MHD equations compared with standard DG methods. The proposed methods in this paper will further show improved performance in some test cases while using the exactly divergence-free magnetic field. Our current methods are formulated only for Cartesian meshes with the second and the third order accuracy. In fact, the second and the third order divergence-free reconstructions in Section 3.2.2 were also used in [2,23], respectively. The extension to unstructured meshes is not trivial. The methods with arbitrarily higher order accuracy however can be formulated and this will be investigated in a forthcoming project, with ideas different from those in [4,24].

The remainder of the paper is organized as follows. In Section 2, we introduce the governing equations, as well as the notations related to meshes and discrete spaces. Section 3 is devoted to the formulation of the numerical methods. It starts with a brief review of the central DG method of Liu et al. [26]. Followed is the proposed method presented first with the forward Euler time discretization and then with the high order time discretizations. Nonlinear limiters, initial and boundary condition treatments are also discussed. In Section 4, numerical experiments are carried out to demonstrate the accuracy and reliability of the methods. There is also a brief discussion on the computational cost. Concluding remarks are made in Section 5. And we summarize formulas for the second and the third order divergence-free reconstructions in Appendix A.

2. Equations, meshes and discrete spaces

2.1. Governing equations

The ideal MHD equations consist of a system of nonlinear hyperbolic equations

$$\frac{\partial \rho}{\partial t} + \nabla \cdot (\rho \mathbf{u}) = 0, \tag{1}$$

$$\frac{\partial(\rho \mathbf{u})}{\partial t} + \nabla \cdot \left[\rho \mathbf{u} \mathbf{u}^\top + \left(p + \frac{1}{2} |\mathbf{B}|^2 \right) \mathbf{I} - \mathbf{B} \mathbf{B}^\top \right] = 0, \tag{2}$$

$$\frac{\partial \mathbf{B}}{\partial t} - \nabla \times (\mathbf{u} \times \mathbf{B}) = 0, \tag{3}$$

$$\frac{\partial \mathcal{E}}{\partial t} + \nabla \cdot \left[\left(\mathcal{E} + p + \frac{1}{2} |\mathbf{B}|^2 \right) \mathbf{u} - \mathbf{B} (\mathbf{u} \cdot \mathbf{B}) \right] = 0 \tag{4}$$

with the additional divergence-free constraint

$$\nabla \cdot \mathbf{B} = 0. \tag{5}$$

Here ρ is the density, p is the hydrodynamic pressure, $\mathbf{u} = (u_x, u_y, u_z)^\top$ is the velocity field, and $\mathbf{B} = (B_x, B_y, B_z)^\top$ is the magnetic field. The total energy \mathcal{E} is given by $\mathcal{E} = \frac{1}{2} \rho |\mathbf{u}|^2 + \frac{1}{2} |\mathbf{B}|^2 + \frac{p}{\gamma-1}$ with γ as the ratio of the specific heats. In addition, \mathbf{I} is the identity matrix and $\nabla = (\frac{\partial}{\partial x}, \frac{\partial}{\partial y})^\top$. Eqs. (1), (2), and (4) come from the conservation of mass, momentum, and energy, respectively. And (3) is the magnetic induction equation system, which can be also written as

$$\frac{\partial \mathbf{B}}{\partial t} + \nabla \times \mathbf{E} = 0, \tag{6}$$

with $\mathbf{E} = -\mathbf{u} \times \mathbf{B}$ being the electric field. Note that if the divergence-free constraint (5) is satisfied initially, it will hold for any future time based on induction equations. Neglecting this constraint in numerical simulations however may lead to non-physical features of approximating solutions or numerical instability [7,31,21,6]. To facilitate our presentation, we rewrite the two-dimensional MHD system (1)–(4) as follows:

$$\frac{\partial \mathbf{U}}{\partial t} + \nabla \cdot \mathbf{F}(\mathbf{U}, \mathcal{B}) = \mathbf{0}, \tag{7}$$

$$\frac{\partial \mathcal{B}}{\partial t} + \nabla \times E_z(\mathbf{U}, \mathcal{B}) = \mathbf{0}, \tag{8}$$

where $\mathbf{U} = (\rho, \rho u_x, \rho u_y, \rho u_z, B_x, B_y, \mathcal{E})^\top$, $\mathcal{B} = (B_x, B_y)^\top$, and $\mathbf{F} = (F_1, F_2)$ with

$$F_1(\mathbf{U}, \mathcal{B}) = \left(\rho u_x, \rho u_x^2 + p + \frac{1}{2} |\mathbf{B}|^2 - B_x^2, \rho u_x u_y - B_x B_y, \rho u_x u_z - B_x B_z, u_x B_z - u_z B_x, u_x \left(\mathcal{E} + p + \frac{1}{2} |\mathbf{B}|^2 \right) - B_x (\mathbf{u} \cdot \mathbf{B}) \right)^\top, \tag{9}$$

$$F_2(\mathbf{U}, \mathcal{B}) = \left(\rho u_y, \rho u_y u_x - B_y B_x, \rho u_y^2 + p + \frac{1}{2} |\mathbf{B}|^2 - B_y^2, \rho u_y u_z - B_y B_z, u_y B_z - u_z B_y, u_y \left(\mathcal{E} + p + \frac{1}{2} |\mathbf{B}|^2 \right) - B_y (\mathbf{u} \cdot \mathbf{B}) \right)^\top. \tag{10}$$

In addition, $E_z(\mathbf{U}, \mathcal{B}) = u_y B_x - u_x B_y$, and it is the z-component of the electric field. And $\nabla \times E_z = \left(\frac{\partial E_z}{\partial y}, -\frac{\partial E_z}{\partial x} \right)^\top$.

2.2. Overlapping meshes and discrete spaces

In this subsection, we introduce meshes, discrete spaces and the relevant notations. Since only Cartesian grids are considered in this paper, without loss of generality we assume the computational domain is $\Omega = (0, a) \times (0, b) \subset \mathbb{R}^d$, with $d = 2$. Let $\{x_i\}_i$ and $\{y_j\}_j$ be partitions of $(0, a)$ and $(0, b)$, respectively, $x_{i+\frac{1}{2}} = \frac{1}{2}(x_i + x_{i+1})$, and $y_{j+\frac{1}{2}} = \frac{1}{2}(y_j + y_{j+1})$. Then $\mathcal{T}_h^c = \{C_{ij}, \forall i, j\}$ and $\mathcal{T}_h^d = \{D_{ij}, \forall i, j\}$ define two overlapping meshes for Ω , with $C_{ij} = (x_i, x_{i+1}) \times (y_j, y_{j+1})$ and $D_{ij} = (x_{i-\frac{1}{2}}, x_{i+\frac{1}{2}}) \times (y_{j-\frac{1}{2}}, y_{j+\frac{1}{2}})$. They are also called primal and dual meshes, respectively. Associated with each mesh, the following discrete spaces are defined

$$\begin{aligned} \mathcal{U}_h^* &= \mathcal{U}_h^{*,k} = \left\{ \mathbf{v} \in [L^2(\Omega)]^{8-d} : \mathbf{v}|_K \in [P^k(K)]^{8-d}, \forall K \in \mathcal{T}_h^* \right\}, \\ \mathcal{M}_h^* &= \mathcal{M}_h^{*,k} = \left\{ \mathbf{v} \in H(\text{div}^0; \Omega) : \mathbf{v}|_K \in \mathcal{W}^k(K), \forall K \in \mathcal{T}_h^* \right\}, \end{aligned}$$

where \star denotes C and D, $P^k(K)$ denotes the space of polynomials in K with the total degree at most k , and

$$\begin{aligned} \mathcal{W}^k(K) &= [P^k(K)]^d \oplus \text{span}\{\nabla \times (x^{k+1}y), \nabla \times (xy^{k+1})\}, \\ H(\text{div}^0; \Omega) &= \{\mathbf{v} \in H(\text{div}; \Omega) : \nabla \cdot \mathbf{v} = 0\}, \\ H(\text{div}; \Omega) &= \{\mathbf{v} \in [L^2(\Omega)]^d : \nabla \cdot \mathbf{v} \in L^2(\Omega)\}. \end{aligned}$$

Note that the functions in $\mathcal{M}_h^{*,k}$ are exactly divergence-free, that is, they are piecewise divergence-free and have continuous normal components across element interfaces. Furthermore, based on [8], $\mathcal{M}_h^{*,k}$ has optimal approximation properties for $H(\text{div}^0; \Omega)$ on Cartesian meshes with respect to the index k .

3. Numerical schemes

3.1. Review of central DG methods of Liu et al. [26]

To better present the exactly divergence-free central DG methods for the MHD system, we first review the central DG method of Liu et al. [26] when it is applied to a one-dimensional scalar conservation equation

$$\frac{\partial u(x, t)}{\partial t} + \frac{\partial f(u(x, t))}{\partial x} = 0, \quad x \in (0, a). \tag{11}$$

The method can also be defined for multi-dimensional or system of hyperbolic conservation laws. Let $\{x_i\}_i$ be a partition of $(0, a)$. With $x_{i+\frac{1}{2}} = \frac{1}{2}(x_i + x_{i+1})$, $I_i = (x_i, x_{i+1})$ and $I_{i+\frac{1}{2}} = (x_{i-\frac{1}{2}}, x_{i+\frac{1}{2}})$, we define two discrete spaces associated with overlapping meshes $\{I_i\}_i$ and $\{I_{i+\frac{1}{2}}\}_i$: $\mathcal{V}_h^c = \mathcal{V}_h^{c,k} = \{v : v|_{I_i} \in P^k(I_i), \forall i\}$, $\mathcal{V}_h^d = \mathcal{V}_h^{d,k} = \{v : v|_{I_{i+\frac{1}{2}}} \in P^k(I_{i+\frac{1}{2}}), \forall i\}$. Here $P^k(I)$ denotes the space of polynomials in I with the degree at most k . To solve (11), the central DG method uses both spaces \mathcal{V}_h^c and \mathcal{V}_h^d and its semi-discrete formulation is given as follows: look for $u_h^c(\cdot, t) \in \mathcal{V}_h^{c,k}$ and $u_h^d(\cdot, t) \in \mathcal{V}_h^{d,k}$, such that for any $v \in P^k(I_i)$, $w \in P^k(I_{i+\frac{1}{2}})$ with any i ,

$$\begin{aligned} \int_{I_i} \frac{\partial u_h^c}{\partial t} v dx &= \frac{1}{\tau_{\max}} \int_{I_i} (u_h^d - u_h^c) v dx + \int_{I_i} f(u_h^d) \frac{\partial v}{\partial x} dx - f(u_h^d(x_{i+1}, t)) v(x_{i+1}) + f(u_h^c(x_i, t)) v(x_i), \\ \int_{I_{i+\frac{1}{2}}} \frac{\partial u_h^d}{\partial t} w dx &= \frac{1}{\tau_{\max}} \int_{I_{i+\frac{1}{2}}} (u_h^c - u_h^d) w dx + \int_{I_{i+\frac{1}{2}}} f(u_h^c) \frac{\partial w}{\partial x} dx - f(u_h^c(x_{i+\frac{1}{2}}, t)) w(x_{i+\frac{1}{2}}) + f(u_h^d(x_{i-\frac{1}{2}}, t)) w(x_{i-\frac{1}{2}}). \end{aligned}$$

Here τ_{\max} is the maximal time step allowed by the CFL restriction. It is more suitable to write $\tau_{\max} = \tau_{\max}(t)$, as τ_{\max} is often dynamically chosen in implementation. The fully discrete central DG method can be obtained if one further discretizes the time variable t . For instance, with the forward Euler time discretization, one has: look for $u_h^{n+1,C} \in \mathcal{V}_h^{C,k}$ and $u_h^{n+1,D} \in \mathcal{V}_h^{D,k}$, such that for any $v \in P^k(I_i)$, $w \in P^k(I_{i+\frac{1}{2}})$ with any i ,

$$\int_{I_i} u_h^{n+1,C} v \, dx = \int_{I_i} (\theta_n u_h^{n,D} + (1 - \theta_n) u_h^{n,C}) v \, dx + \Delta t_n \left(\int_{I_i} f(u_h^{n,D}) \frac{\partial v}{\partial x} \, dx - f(u_h^{n,D}(x_{i+1}, t)) v(x_{i+1}) + f(u_h^{n,D}(x_i, t)) v(x_i) \right),$$

$$\int_{I_{i+\frac{1}{2}}} u_h^{n+1,D} w \, dx = \int_{I_{i+\frac{1}{2}}} (\theta_n u_h^{n,C} + (1 - \theta_n) u_h^{n,D}) w \, dx + \Delta t_n \left(\int_{I_{i+\frac{1}{2}}} f(u_h^{n,C}) \frac{\partial w}{\partial x} \, dx - f(u_h^{n,C}(x_{i+\frac{1}{2}}, t)) w(x_{i+\frac{1}{2}}) + f(u_h^{n,C}(x_{i-\frac{1}{2}}, t)) w(x_{i-\frac{1}{2}}) \right).$$

Here $u_h^{n,C} \in \mathcal{V}_h^{C,k}$ and $u_h^{n,D} \in \mathcal{V}_h^{D,k}$ approximate the solution of (11) at $t = t_n$, and $u_h^{n+1,C}$ and $u_h^{n+1,D}$ approximate the solution at $t_{n+1} = t_n + \Delta t_n$. In addition, $\theta_n = \Delta t_n / \tau_n \in [0, 1]$ with $\tau_n = \tau_{\max}(t_n)$. High order time discretizations can be used for better accuracy in temporal direction. Stability should be considered when one chooses the time discretization to get a fully discrete scheme (see e.g Table 6 in [27]). Note that with two copies of numerical solutions, the method does not need numerical fluxes which are exact or approximate Riemann solvers and are used in standard DG methods [11]. This feature is shared by central type schemes, e.g. [1,23].

3.2. Schemes with the forward Euler time discretization

In this section, we formulate the second and the third order central DG methods with the exactly divergence-free magnetic field to solve the system (7) and (8) and therefore (1)–(4). The methods evolve two copies of numerical solutions. Let us assume they are available at $t = t_n$, denoted as $(\mathbf{U}_h^{n,\star}, \mathcal{B}_h^{n,\star}) \in \mathcal{U}_h^{\star,k} \times \mathcal{M}_h^{\star,k}$ with $\mathcal{B}_h^{n,\star} = (\mathcal{B}_{x,h}^{n,\star}, \mathcal{B}_{y,h}^{n,\star})$. Here and below \star denotes C and D. We will describe how to obtain two sets of numerical solutions at $t_{n+1} = t_n + \Delta t_n$, denoted as $(\mathbf{U}_h^{n+1,\star}, \mathcal{B}_h^{n+1,\star}) \in \mathcal{U}_h^{\star,k} \times \mathcal{M}_h^{\star,k}$ with $\mathcal{B}_h^{n+1,\star} = (\mathcal{B}_{x,h}^{n+1,\star}, \mathcal{B}_{y,h}^{n+1,\star})$. Due to similarity, we only present the procedure to update $(\mathbf{U}_h^{n+1,C}, \mathcal{B}_h^{n+1,C})$. We start with the first order forward Euler time discretization, and higher order time discretizations will be discussed afterward.

3.2.1. Updating $\mathbf{U}_h^{n+1,C}$

To get $\mathbf{U}_h^{n+1,C}$, we apply to (7) the central DG methods of Liu et al. [26] as the spatial discretization and the forward Euler method as the time discretization. That is, to look for $\mathbf{U}_h^{n+1,C} \in \mathcal{U}_h^{C,k}$, such that for any $\mathbf{V} \in [P^k(C_{ij})]^{8-d}$ with any i, j ,

$$\int_{C_{ij}} \mathbf{U}_h^{n+1,C} \cdot \mathbf{V} \, dx = \int_{C_{ij}} (\theta_n \mathbf{U}_h^{n,D} + (1 - \theta_n) \mathbf{U}_h^{n,C}) \cdot \mathbf{V} \, dx + \Delta t_n \left(\int_{C_{ij}} \mathbf{F}(\mathbf{U}_h^{n,D}, \mathcal{B}_h^{n,D}) \cdot \nabla \mathbf{V} \, dx - \int_{\partial C_{ij}} (\mathbf{F}(\mathbf{U}_h^{n,D}, \mathcal{B}_h^{n,D}) \cdot \mathbf{n}) \cdot \mathbf{V} \, ds \right), \tag{12}$$

Here $\theta_n = \Delta t_n / \tau_n \in [0, 1]$, with τ_n being the maximal time step allowed by the CFL restriction [26] at t_n . And \mathbf{n} is the unit outward normal along ∂C_{ij} .

3.2.2. Updating the exactly divergence-free $\mathcal{B}_h^{n+1,C}$

Note a piecewise divergence-free vector field is exactly (or called globally) divergence-free if and only if it has continuous normal component across element interfaces. Therefore our next step to get the exactly divergence-free $\mathcal{B}_h^{n+1,C}$ starts with first approximating the normal component of the magnetic field $\mathbf{n} \cdot \mathcal{B}$ on the mesh skeleton, namely, the mesh interfaces, then an element by element divergence-free reconstruction follows with the matching accuracy. This procedure is related to the constraint transport methodology [16] which uses the magnetic flux as a fundamental variable and works with the induction equation system in its integral form. For the Cartesian mesh we are considering, the normal component of \mathcal{B} on the mesh skeleton is determined by B_x along y-direction edges and B_y along x-direction edges.

We first discretize the two one-dimensional equations of the system (8)

$$\frac{\partial B_x}{\partial t} = - \frac{\partial E_z}{\partial y}, \tag{13}$$

$$\frac{\partial B_y}{\partial t} = \frac{\partial E_z}{\partial x}, \tag{14}$$

with respect to the primal mesh \mathcal{T}_h^C as follows: for any i, j , look for $b_{x,i}^C(y) \in P^k((y_j, y_{j+1}))$ such that

$$\int_{y_j}^{y_{j+1}} b_{x,i}^C(y)\mu(y)dy = \int_{y_j}^{y_{j+1}} \left(\theta_n B_{x,h}^{n,D}(x_i,y) + (1 - \theta_n) B_{x,h}^{n,C}(x_i,y) \right) \mu(y) dy + \Delta t_n \left(- \int_{y_j}^{y_{j+1}} E_z^{n,D}(x_i,y) \frac{\partial \mu(y)}{\partial y} dy - E_{z,i,j+1}^{n,D} \mu(y_{j+1}) + E_{z,i,j}^{n,D} \mu(y_j) \right), \tag{15}$$

for any $\mu(y) \in P^k(\mathbb{R})$, and look for $b_{y,j}^C(x) \in P^k((x_i, x_{i+1}))$ such that

$$\int_{x_i}^{x_{i+1}} b_{y,j}^C(x)v(x)dx = \int_{x_i}^{x_{i+1}} \left(\theta_n B_{y,h}^{n,D}(x,y_j) + (1 - \theta_n) B_{y,h}^{n,C}(x,y_j) \right) v(x) dx + \Delta t_n \left(- \int_{x_i}^{x_{i+1}} E_z^{n,D}(x,y_j) \frac{\partial v(x)}{\partial x} dx + E_{z,i+1,j}^{n,D} v(x_{i+1}) - E_{z,i,j}^{n,D} v(x_i) \right), \tag{16}$$

for any $v(x) \in P^k(\mathbb{R})$. Here $E_z^{n,D}(x,y) = E_z(\mathbf{U}_h^{n,D}(x,y), \mathcal{B}_h^{n,D}(x,y))$ and $E_{z,i,j}^{n,D} = E_z^{n,D}(x_i,y_j)$ for any i and j . And θ_n is the same as before.

The scheme above can be regarded as central DG methods applied to one-dimensional problems (13) and (14) with the meshes derived from the skeletons of \mathcal{T}_h^C and \mathcal{T}_h^D . Moreover, $b_{x,i}^C$ and $b_{y,j}^C$ provide approximations for $B_x(x_i,y)$ and $B_y(x,y_j)$ at t_{n+1} , and they satisfy the following compatibility condition:

$$\int_{y_j}^{y_{j+1}} b_{x,i+1}^C dy - \int_{y_j}^{y_{j+1}} b_{x,i}^C dy + \int_{x_i}^{x_{i+1}} b_{y,j+1}^C dx - \int_{x_i}^{x_{i+1}} b_{y,j}^C dx = 0 \tag{17}$$

for any given i and j . Now we want to verify (17) which is a necessary condition for the divergence-free reconstruction in the next step. Take $\mu(y) \equiv 1$ in (15), with the index i being $i + 1$ and i , we have

$$\int_{y_j}^{y_{j+1}} b_{x,i+1}^C(y)dy = \int_{y_j}^{y_{j+1}} \left(\theta_n B_{x,h}^{n,D}(x_{i+1},y) + (1 - \theta_n) B_{x,h}^{n,C}(x_{i+1},y) \right) dy + \Delta t_n \left(-E_{z,i+1,j+1}^{n,D} + E_{z,i+1,j}^{n,D} \right),$$

$$\int_{y_j}^{y_{j+1}} b_{x,i}^C(y)dy = \int_{y_j}^{y_{j+1}} \left(\theta_n B_{x,h}^{n,D}(x_i,y) + (1 - \theta_n) B_{x,h}^{n,C}(x_i,y) \right) dy + \Delta t_n \left(-E_{z,i,j+1}^{n,D} + E_{z,i,j}^{n,D} \right).$$

Take $v(x) \equiv 1$ in (16), with the index j being $j + 1$ and j , we have

$$\int_{x_i}^{x_{i+1}} b_{y,j+1}^C(x)dx = \int_{x_i}^{x_{i+1}} \left(\theta_n B_{y,h}^{n,D}(x,y_{j+1}) + (1 - \theta_n) B_{y,h}^{n,C}(x,y_{j+1}) \right) dx + \Delta t_n \left(E_{z,i+1,j+1}^{n,D} - E_{z,i,j+1}^{n,D} \right),$$

$$\int_{x_i}^{x_{i+1}} b_{y,j}^C(x)dx = \int_{x_i}^{x_{i+1}} \left(\theta_n B_{y,h}^{n,D}(x,y_j) + (1 - \theta_n) B_{y,h}^{n,C}(x,y_j) \right) dx + \Delta t_n \left(E_{z,i+1,j}^{n,D} - E_{z,i,j}^{n,D} \right).$$

Then

$$\int_{y_j}^{y_{j+1}} b_{x,i+1}^C(y)dy - \int_{y_j}^{y_{j+1}} b_{x,i}^C(y)dy + \int_{x_i}^{x_{i+1}} b_{y,j+1}^C(x)dx - \int_{x_i}^{x_{i+1}} b_{y,j}^C(x)dx = \int_{\partial C_{ij}} \left(\theta_n \mathbf{n} \cdot \mathcal{B}_h^{n,D} + (1 - \theta_n) \mathbf{n} \cdot \mathcal{B}_h^{n,C} \right) ds$$

$$= \int_{C_{ij}} \left(\theta_n \nabla \cdot \mathcal{B}_h^{n,D} + (1 - \theta_n) \nabla \cdot \mathcal{B}_h^{n,C} \right) \mathbf{dx} = 0,$$

and this gives (17). The derivation has used the fact that both $\mathcal{B}_h^{n,C}$ and $\mathcal{B}_h^{n,D}$ at t_n are exactly divergence-free. In addition, the electric flux $\{E_{z,i,j}^{n,D}\}_{i,j}$, used to discretize the induction equations (15) and (16), are evaluated based on the numerical solution on the dual mesh, they are naturally single-valued at the grid-points of the primal mesh, and therefore all relevant terms are canceled out with each other. We want to comment that in Godunov type methods such as [5,4,17], additional interpolation or averaging procedure is needed to produce a single-valued electric magnetic flux and therefore to result in (17), and certain upwind mechanism needs to be incorporated for stability consideration especially for high order schemes.

The final step of the proposed methods is an element-by-element divergence-free reconstruction to define $\mathcal{B}_h^{n+1,C} = \left(\mathcal{B}_{x,h}^{n+1,C}, \mathcal{B}_{y,h}^{n+1,C} \right)$. Given i, j , the reconstruction on C_{ij} goes as: look for $\mathcal{B}_h^{n+1,C}|_{C_{ij}} \in \mathcal{V}^k(C_{ij})$ such that

- $\mathcal{B}_{x,h}^{n+1,C}(x_i,y) = b_{x,i}^C(y)$ for $l = i, i + 1$ and $y \in (y_j, y_{j+1})$,
- $\mathcal{B}_{y,h}^{n+1,C}(x,y_l) = b_{y,l}^C(x)$ for $l = j, j + 1$ and $x \in (x_i, x_{i+1})$,
- $\nabla \cdot \mathcal{B}_h^{n+1,C}|_{C_{ij}} = 0$.

For $k = 1$ and $k = 2$, the reconstruction defined above is uniquely determined provided that the compatibility condition (17) holds. As the reconstruction was also used in [2] for $k = 1$ and [23] for $k = 2$, we will not repeat the derivation but include the algebraic formulas in Appendix A. Now $\mathcal{B}_h^{n+1,C}$ is piecewise divergence-free with respect to the primal mesh \mathcal{T}_h^C , and its normal components along the mesh interfaces are continuous. Therefore $\mathcal{B}_h^{n+1,C}$ is exactly divergence-free and $\mathcal{B}_h^{n+1,C} \in \mathcal{M}_h^{C,k}$.

Moreover, when $k = 1$ and $k = 2$, respectively, $\mathcal{B}_h^{n+1,C}$ is the second and the third order approximation for the magnetic field [8]. For $k > 2$, more information about \mathcal{B} than its normal component on the mesh skeleton is needed to determine the reconstruction, and this will be investigated in our forthcoming project.

3.3. Schemes with high order time discretizations

So far the algorithm is presented when the first order forward Euler method is taken as the time discretization. To increase the accuracy in time, strong stability preserving (SSP) high order Runge–Kutta or multi-step [19] time discretizations can be used. Such discretization is a convex combination of the forward Euler method, and therefore the full scheme with a high order SSP time discretization will still produce an exactly divergence-free approximation for the magnetic field. For multi-stage time discretizations such as SSP Runge–Kutta methods, one needs to apply the divergence-free reconstruction for each inner stage. For the numerical experiments in Section 4, the third order total variation diminishing (TVD) Runge–Kutta method [12] is applied.

3.4. Nonlinear limiter, initial and boundary conditions

Similar to other high order methods for nonlinear hyperbolic conservation laws, nonlinear limiters are needed for numerical stability in some test examples. In our simulation, the total variation bounded (TVB) minmod slope limiter [30,12] is taken. This simple limiter involves a positive parameter M . It is known that for smooth examples, one needs to choose a suitable M (for instance with a large enough M to turn off this limiter) or to adopt other limiting strategies [29,25] in order to keep the designed accuracy. We here choose not to apply the limiter to smooth examples, and set $M = 1$ for the remaining test cases. Different values of M or other limiters [29,25] may produce better results for each individual example, and this will not be explored in this paper. The limiter can be implemented either componentwisely or in local characteristic fields, and its performance with these implementations will be commented for each example. Finally, we want to mention that *no limiting procedure* is applied to the magnetic field computed in Section 3.2.2.

The numerical solutions are initialized through the L^2 projections of the initial condition onto $\mathcal{U}_h^{C,k} \times \mathcal{M}_h^{C,k}$ and $\mathcal{U}_h^{D,k} \times \mathcal{M}_h^{D,k}$, respectively. And this makes the simulation start with the exactly divergence-free magnetic field approximation. For the periodic boundary condition, the treatment is straightforward. For the outgoing boundary condition, ghost cells are used, and the numerical solution is extrapolated such that the electric field flux used to discretize equations (13) and (14) is single-valued at the grid-points, and the magnetic field is exactly divergence-free. These will lead to the compatibility condition (17) which is necessary for the divergence-free reconstructions. For general boundary conditions, complexity arises due to the use of overlapping meshes and the requirement for the magnetic field to be exactly divergence-free, and this will not be investigated in this paper.

4. Numerical examples

In this section, numerical examples are presented to demonstrate the performance of the proposed methods. We start with three smooth examples, namely, an essentially “scalar” example, the smooth Alfvén wave problem, and the smooth vortex problem, to show the accuracy of the schemes. Then our methods are tested through the field loop advection, the Orszag–Tang vortex example, and the rotor problem which all involve periodic boundary conditions. Finally we consider the Brio–Wu shock-tube problem in unrotated and rotated two-dimensional frames, the blast problem and the cloud-shock interaction example with outgoing boundary conditions. In the simulation, the primal mesh is taken as the uniform rectangular mesh. We use P^k approximations to denote the solutions computed with the discrete spaces $\mathcal{U}_h^{C,k} \times \mathcal{M}_h^{C,k}$ and $\mathcal{U}_h^{D,k} \times \mathcal{M}_h^{D,k}$. The time step Δt is dynamically determined by

$$\Delta t = \frac{C_{cfl}}{\left(\frac{\max(|u_x| + c_f^x)}{\Delta x} + \frac{\max(|u_y| + c_f^y)}{\Delta y} \right)},$$

where C_{cfl} defines the CFL number, c_f^x and c_f^y are the fast speed in x and y directions, respectively (see [28] for the definition), and the maxima are computed over all cell elements. With the third order TVD Runge–Kutta time discretization [12], we take $C_{cfl} = 1.0$ for $k = 1$ and $C_{cfl} = 0.6$ for $k = 2$ unless otherwise indicated. And $\theta_n = 1$ is used with $\tau_n = \Delta t_n$. As suggested in [27], it is observed that our methods allow larger CFL number C_{cfl} than standard DG methods with the same Runge–Kutta time discretization. For instance, when solving the smooth examples in Section 4.1, DG methods in [21] with the third order Runge–Kutta time discretization [12] allows $C_{cfl} = 0.75$ for $k = 1$ and $C_{cfl} = 0.3$ for $k = 2$. And they are unstable with $C_{cfl} = 0.78$ for $k = 1$ and with $C_{cfl} = 0.33$ for $k = 2$ when applied to the first smooth example in Section 4.1.1. To save space, the data generated from these numerical experiments will not be included in this paper. For the same reason, except the smooth examples, only P^2 results on the primal mesh are reported below with the consideration that the numerical stability is relatively harder to achieve for higher order methods, although all simulations are performed with both P^1 and P^2 approximations.

4.1. Examples with smooth solutions

4.1.1. The smooth “scalar” example

The first smooth example is essentially a scalar problem, as there is only one nontrivial component ρ in the solution. The simulation starts with the initial condition $(\rho, u_x, u_y, u_z, B_x, B_y, B_z, p) = (2 + \sin(x + y), 1, 1, 0, 0, 0, 0, 5)$ with $\gamma = 2$ in the domain $[0, 2\pi] \times [0, 2\pi]$. Periodic boundary conditions are used, and no nonlinear limiter is applied. The exact solution is simply $\rho(x, y, t) = 2 + \sin(x + y - (u_x + u_y)t) = 2 + \sin(x + y - 2t)$ with other components remaining invariant. The L^2 errors and orders of accuracy are presented in Table 1 for the density ρ at $t = 7$. The results show that the proposed methods are $(k + 1)$ st order accurate for P^k approximations with $k = 1, 2$, and therefore they are optimal with respect to the approximation properties of discrete spaces. Note that this example only involves the hydrodynamical part of the MHD system, and it cannot fully demonstrate the performance of our methods.

4.1.2. The smooth Alfvén wave

The next smooth example describes a circularly polarized Alfvén wave ([31,23]) moving in the domain $[0, 1/\cos\alpha] \times [0, 1/\sin\alpha]$. Here, α represents the angle with respect to the x -axis at which the wave propagates. We use the same initial conditions as [23], that is

$$\begin{aligned} \rho &= 1, & u_{\parallel} &= 0, & u_{\perp} &= 0.1 \sin(2\pi\beta), & u_z &= 0.1 \cos(2\pi\beta), \\ B_{\parallel} &= 1, & B_{\perp} &= u_{\perp}, & B_z &= u_z, & p &= 0.1, \end{aligned}$$

where $\beta = x \cos\alpha + y \sin\alpha$ and $\alpha = \pi/4$. The subscript \parallel and \perp denote the directions parallel and perpendicular to the wave propagation direction, respectively. The boundary conditions are periodic. The Alfvén wave travels towards the origin $(0, 0)$ with a constant Alfvén speed $B_{\parallel}/\sqrt{\rho} = 1$ and it returns to its initial configuration whenever t becomes an integer. In the simulation, $\gamma = 5/3$ is taken and no nonlinear limiter is applied. In Table 2, we report the arithmetic means of the L^2 errors for $u_{\perp}, u_z, B_{\perp}$ and B_z , and the corresponding orders of accuracy at $t = 5$. The results show that the proposed methods are $(k + 1)$ st order accurate for P^k approximations with $k = 1, 2$, and therefore they are optimal. The same conclusion can be drawn based on the convergence order of each physical component.

4.1.3. The smooth vortex problem

The third smooth example is introduced in [3], and the exact solution describes a smooth vortex propagating stably with the speed $(1, 1)$. The simulation is initialized with a background flow $(\rho, u_x, u_y, u_z, B_x, B_y, B_z, p) = (1, 1, 1, 0, 0, 0, 0, 1)$ containing a vortex, which is inducted through the fluctuation in the magnetic and velocity fields given as

$$(\delta u_x, \delta u_y) = \frac{\xi}{2\pi} \nabla \times \exp\{0.5(1 - r^2)\}, \quad (\delta B_x, \delta B_y) = \frac{\eta}{2\pi} \nabla \times \exp\{0.5(1 - r^2)\},$$

and the perturbation in pressure given as

$$\delta p = \frac{\eta^2(1 - r^2) - \xi^2}{8\pi^2} \exp(1 - r^2).$$

Here $r = \sqrt{x^2 + y^2}$. In the simulation, we set $\xi = 1, \eta = 1, \gamma = 5/3$, and use $[-5, 5] \times [-5, 5]$ as the computational domain with the periodic boundary conditions. Such boundary conditions will introduce an error with the magnitude $O(e^{-12}) = O(10^{-6})$

Table 1
 L^2 errors and orders of accuracy of ρ for the smooth scalar problem computed within $[0, 2\pi] \times [0, 2\pi]$ at $t = 7$.

Mesh	p^1		p^2	
	L^2 error	Order	L^2 error	Order
32×32	2.73E-02		6.17E-04	
64×64	5.01E-03	2.45	7.65E-05	3.01
128×128	1.11E-03	2.18	9.55E-06	3.00
256×256	2.67E-04	2.05	1.19E-06	3.00
512×512	6.61E-05	2.02	1.49E-07	3.00

Table 2
 L^2 errors and orders of accuracy for the smooth Alfvén wave problem at $t = 5$.

Mesh	p^1		p^2	
	L^2 error	Order	L^2 error	Order
16×16	6.07E-03	–	1.48E-03	–
32×32	8.43E-04	2.85	1.82E-04	3.02
64×64	1.32E-04	2.68	2.26E-05	3.01
128×128	2.59E-05	2.35	2.83E-06	3.00
256×256	5.97E-06	2.11	3.54E-07	3.00

Table 3

L^2 errors and orders of accuracy of ρ , u_x , B_x and p for the smooth vortex example at $t = 20$. $C_{cfl} = 1.0$ for P^1 approximations and $C_{cfl} = 0.6$ for P^2 approximations.

Mesh	ρ		u_x		B_x		p	
	L^2 error	Order						
P^1								
32×32	1.35E-03	–	2.91E-02	–	2.82E-02	–	5.41E-03	–
64×64	3.21E-04	2.07	4.38E-03	2.74	4.16E-03	2.76	8.85E-04	2.61
128×128	6.12E-05	2.39	5.97E-04	2.87	5.52E-04	2.91	1.37E-04	2.70
256×256	1.30E-05	2.23	8.97E-05	2.74	7.73E-05	2.84	2.53E-05	2.44
P^2								
32×32	1.39E-03	–	3.75E-03	–	1.22E-02	–	2.06E-03	–
64×64	1.86E-04	2.90	4.98E-04	2.91	1.61E-03	2.93	2.80E-04	2.88
128×128	2.34E-05	2.99	6.27E-05	2.99	2.02E-04	2.99	3.53E-05	2.99
256×256	2.92E-06	3.00	7.94E-06	2.98	2.54E-05	2.99	4.41E-06	3.00

Table 4

L^2 errors and orders of accuracy of ρ , u_x , B_x and p for the smooth vortex example at $t = 20$. $C_{cfl} = 0.4$ for P^1 approximations and $C_{cfl} = 0.3$ for P^2 approximations.

Mesh	ρ		u_x		B_x		p	
	L^2 error	Order						
P^1								
32×32	1.81E-03	–	5.17E-02	–	5.12E-02	–	9.14E-03	–
64×64	5.17E-04	1.81	8.60E-03	2.59	8.48E-03	2.60	1.65E-03	2.47
128×128	8.43E-05	2.62	1.15E-03	2.91	1.12E-03	2.92	2.23E-04	2.89
256×256	1.17E-05	2.84	1.52E-04	2.92	1.45E-04	2.95	2.97E-05	2.91
P^2								
32×32	2.51E-03	–	6.68E-03	–	2.23E-02	–	3.76E-03	–
64×64	3.62E-04	2.79	9.64E-04	2.79	3.12E-03	2.84	5.49E-04	2.77
128×128	4.61E-05	2.97	1.23E-04	2.97	3.96E-04	2.98	7.01E-05	2.97
256×256	5.77E-06	3.00	1.55E-05	2.99	4.96E-05	3.00	8.78E-06	3.00

which will not affect the reported results. In addition, no nonlinear limiter is applied. In Table 3, we present the L^2 errors and orders of accuracy for representative variables ρ , u_x , B_x and p at $t = 20$. The results confirm the optimal accuracy orders of our proposed methods.

For all three smooth examples we have tested, it is observed that using relatively smaller CFL numbers and therefore smaller time steps does not always reduce the numerical errors. This is most pronounced in the smooth vortex example, and can be illustrated with Table 4 when $C_{cfl} = 0.4$ for $k = 1$ and $C_{cfl} = 0.3$ for $k = 2$. Indeed, for this example, the errors of most components are smaller on the tested meshes when larger time steps are used.

4.2. Examples with non-smooth solutions

4.2.1. The field loop advection

In this subsection, we consider the magnetic field loop advection problem originally proposed in [17]. The same initial condition as in [23] is used. That is, $(\rho, u_x, u_y, u_z, B_z, p) = (1, 2, 1, 1, 0, 1)$, and $(B_x, B_y) = \nabla \times A_z$, where A_z is the z-component of the magnetic potential

$$A_z = \begin{cases} A_0(R - r) & \text{if } r \leq R, \\ 0 & \text{if } r > R \end{cases}$$

with $A_0 = 10^{-3}$, $R = 0.3$ and $r = \sqrt{x^2 + y^2}$. The methods are implemented on the 200×100 mesh of the computational domain $[-1, 1] \times [-0.5, 0.5]$. We take $\gamma = 5/3$ and the boundary conditions are periodic.

The gray-scale images of the magnetic pressure $B_x^2 + B_y^2$ in the solution, which is convected across the domain periodically, are shown in Fig. 1. They are based on the initial condition at $t = 0$ and the P^2 approximation at $t = 2$. The field loop is well preserved in the simulation. And similar as in [17,23], numerical dissipation is observed around the center and the boundary of the loop. Unlike some schemes discussed in [17,23], our exactly divergence-free methods do not produce oscillatory solutions. In Fig. 2, we further show the magnetic field lines. Due to the exactly divergence-free feature of our computed magnetic field, the magnetic field lines are plotted by contouring the z-component of the numerical magnetic potential A_z . It is observed that the symmetry is well preserved at $t = 2$ and even at later time $t = 10$. The slight distortion at $t = 10$ can be expected due to the numerical dissipation in the long time simulation. All presented results are computed with the

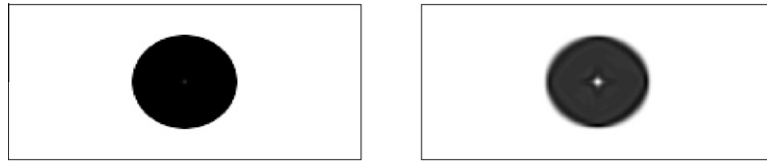


Fig. 1. The magnetic pressure $B_x^2 + B_y^2$ of the field loop advection. P^2 approximation on the 200×100 mesh. Left: $t = 0$; right: $t = 2$.

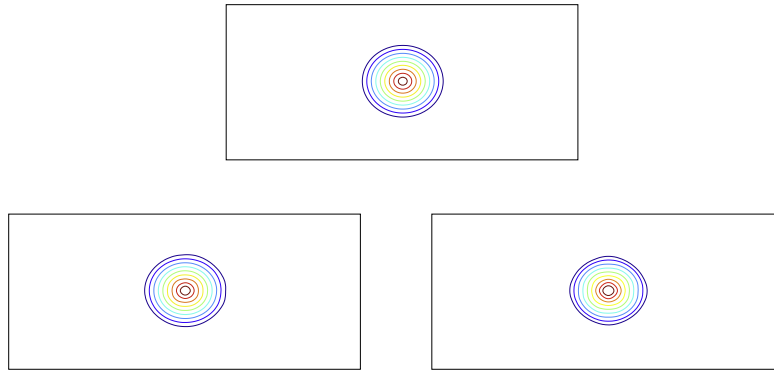


Fig. 2. The magnetic field lines of the field loop advection. P^2 approximations on the 200×100 mesh. Uniform range are used for all three plots. Top: $t = 0$; bottom left: $t = 2$; bottom right: $t = 10$.

componentwise limiter, and there is no visible difference in the results when the limiter is implemented in the local characteristic fields. As a final remark, though “whether the z -component of the magnetic field B_z stays around machine zero” was used in [23] to demonstrate the importance of the magnetic field being divergence-free in the simulation, our methods produce the approximated B_z with the magnitude of 10^{-7} while using the exactly divergence-free magnetic field. This can be explained by the $O(10^{-6})$ deviation of the numerical u_z from its exact value 1.

4.2.2. The Orszag–Tang vortex problem

In this subsection, we consider the Orszag–Tang vortex problem. This is a widely used test example and it involves formation and interaction of multiple shocks as the nonlinear system evolves. The same initial condition as in [21] is taken, that is,

$$\begin{aligned} \rho &= \gamma^2, & u_x &= -\sin y, & u_y &= \sin x, & u_z &= 0, \\ B_x &= -\sin y, & B_y &= \sin 2x, & B_z &= 0, & p &= \gamma \end{aligned}$$

with $\gamma = 5/3$. The computational domain is $[0, 2\pi] \times [0, 2\pi]$ with the periodic boundary conditions. In Fig. 3, we show the time evolution of the density ρ at times $t = 0.5, 2, 3$, and 4, respectively. The simulation is based on P^2 approximations on the 192×192 mesh. The solution is smooth initially, and it grows more complicated as the time progresses. Our results are in good agreement with those in , e.g. [21,24].

As indicated in [21], different schemes, or even the same scheme with various solution spaces may behave quite differently for this example in terms of their ability to keep the simulation from breaking down. One explanation is that the numerical divergence error can lead to numerical instability [21,24]. With the proposed methods, the computation with P^1 and P^2 approximations stays stable till at least $t = 30$ (the maximum time we run, and the simulation can still continue). And the time length for the P^2 simulation to be stable is much longer than that of the locally divergence-free DG method in [21]. This indicates that our exactly divergence-free central DG methods have better numerical stability compared with locally divergence-free DG methods in [21], where the divergence error is only partially removed by using special discrete spaces. This also provides evidence that the divergence error has contribution to the numerical stability of the schemes.

We further perform a convergence study for the proposed methods using this example. In particular, the simulations are carried out on 192×192 and 384×384 meshes till $t = 2$ when non-smooth features have already formed. In Fig. 4, we plot the pressure p at $x = 1.9635$ based on P^2 approximations. With the shock developed in the solution, the convergence can be observed. For comparison, we also include the pressure cuts of the locally divergence-free DG method [21] in Fig. 4, and the two sets of plots are nearly the same. The reported results are obtained when the componentwise limiter is used as it generates slightly smaller oscillation. Finally, we want to point out that no negative pressure is produced throughout the simulation.

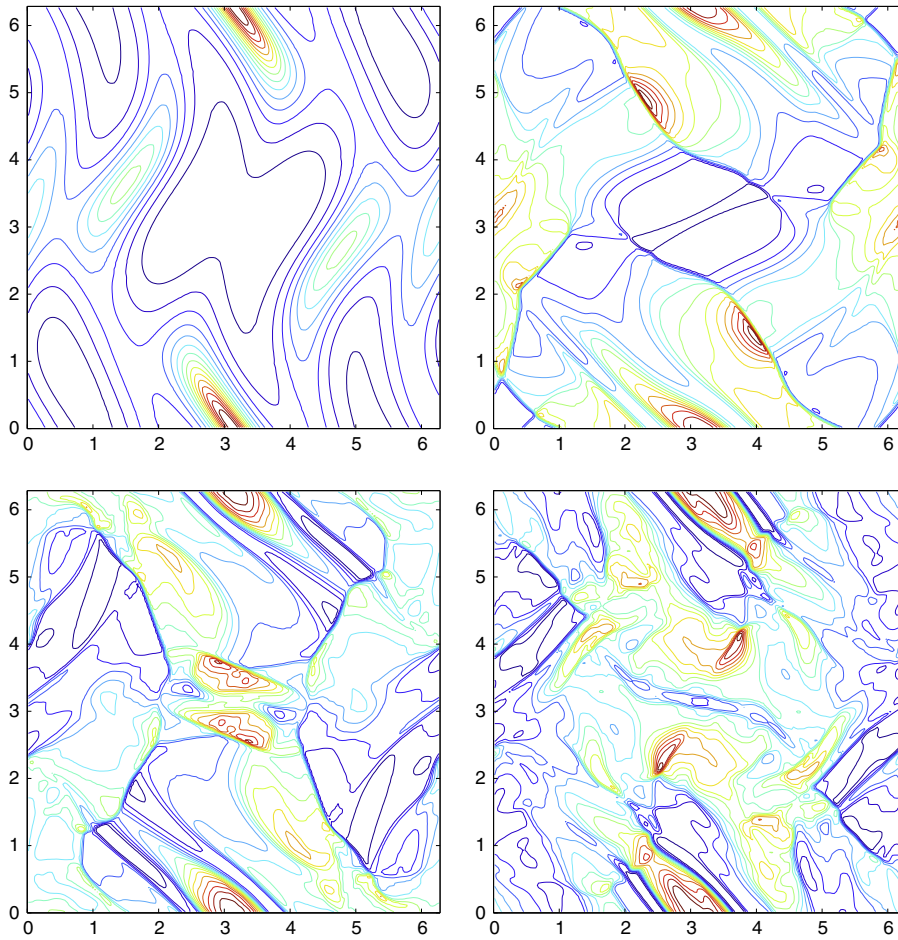


Fig. 3. Development of the density ρ in Orszag–Tang vortex problem at $t = 0.5$ (top left), $t = 2$ (top right), $t = 3$ (bottom left), and $t = 4$ (bottom right). P^2 approximation on the 192×192 mesh. Fifteen equally spaced contours with ranges $[2.11, 5.82]$, $[0.62, 6.41]$, $[1.16, 6.12]$, and $[1.25, 5.78]$, respectively.

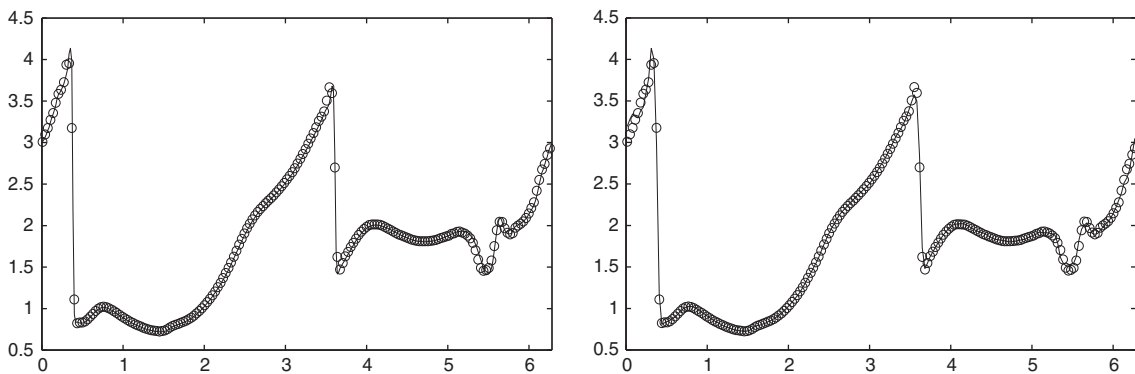


Fig. 4. The pressure p in Orszag–Tang vortex problem with $x = 1.9635$ at $t = 2$. P^2 approximations on the 192×192 mesh (circle) and the 384×384 mesh (solid line). Left: the proposed method; right: the locally divergence-free DG method in [21].

4.2.3. The rotor problem

We next consider the rotor problem which was explained in details in [5]. The problem describes a dense disk of fluid rapidly spinning in a light ambient fluid. A “taper” function is used to bridge these two areas to reduce the initial transition. Following [31], the starting setup is given as

$$(u_z, B_x, B_y, B_z, p) = (0, 5/\sqrt{4\pi}, 0, 0, 0.5),$$

and

$$(\rho, u_x, u_y) = \begin{cases} (10, -(y-0.5)/r_0, (x-0.5)/r_0) & \text{if } r < r_0 \\ (1+9\lambda, -\lambda(y-0.5)/r, \lambda(x-0.5)/r) & \text{if } r_0 < r < r_1 \\ (1, 0, 0) & \text{if } r > r_1 \end{cases}$$

with $r = \sqrt{(x-0.5)^2 + (y-0.5)^2}$, $r_0 = 0.1$, $r_1 = 0.115$ and $\lambda = (r_1 - r)/(r_1 - r_0)$. The simulation is implemented in the domain $[0, 1] \times [0, 1]$, and periodic boundary conditions are used with $\gamma = 5/3$. When the limiter is applied, we use the TVB minmod limiter implemented in the local characteristic fields, which performs much better than the componentwise one.

In Fig. 5, we show the contour plots of P^2 approximations at $t = 0.295$ on a 200×200 mesh. In particular, they are for density ρ , pressure p , the hydrodynamic Mach number $|\mathbf{u}|/c$ (with $c = \sqrt{\gamma p/\rho}$ being the sound speed), and the magnetic pressure $|\mathbf{B}|^2/2$. Similar to [5,31,21], we further examine the performance of the methods by zooming in the central part of the Mach number, see Fig. 6. Note that there is no “distortion” in the numerical solutions, and such distortion was reported in [31,21] and was attributed to the divergence error in the magnetic field. It was reported in [31] that many one step TVD based schemes failed for this problem due to the negative pressure, however in our simulation, there is no negative pressure observed.

For this example, with the moderately reduced CFL number, our methods produce satisfactory approximations even when the limiter is not applied. This observation is illustrated by P^2 approximations with $C_{fl} = 0.3$ in Fig. 7, which include the zoom-in plots of the central part of the Mach number at $t = 0.295$ with and without using the limiter. When the mesh is refined, the difference between these two groups of numerical solutions is diminishing, and this indicates good stability property of the proposed methods. For the relatively coarser grids, the limiter improves the solutions by removing the oscillations along the edge of the central “ellipse” of the Mach number. We further perform a convergence study for our method with and without using the limiter. In Fig. 8, we plot the Mach number at $x = 0.413$ from the P^2 approximations on 400×400 and 800×800 meshes, and they are nearly the same as those by the locally divergence-free DG method (see Fig. 19 of [21]). With

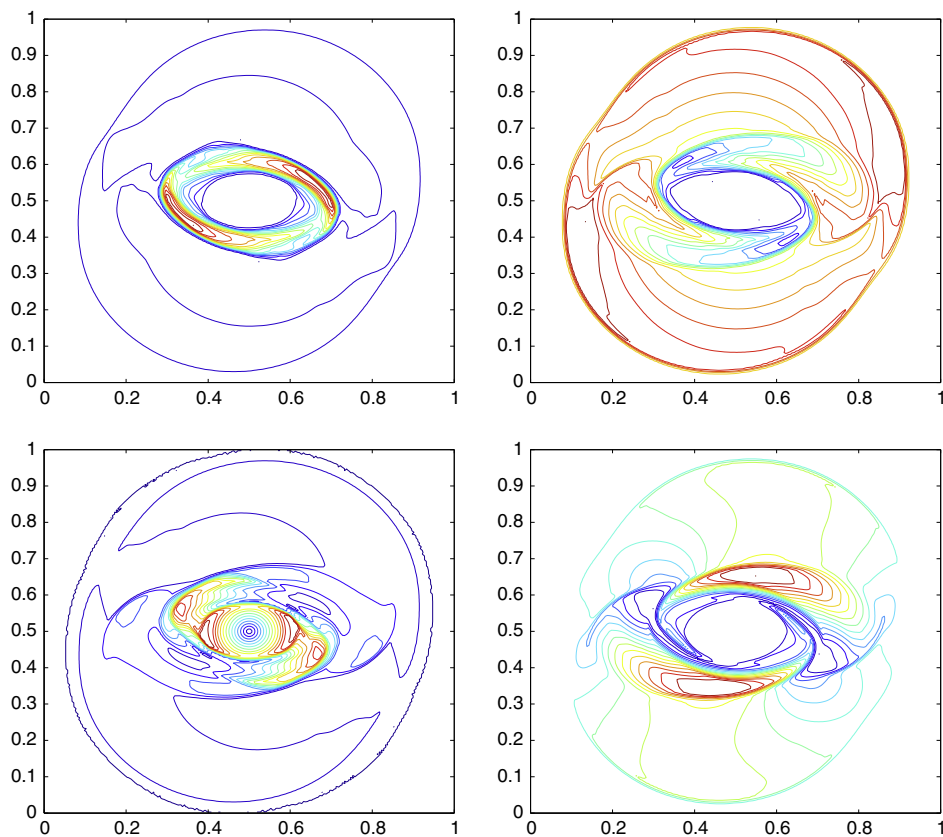


Fig. 5. P^2 approximations for the rotor problem on the 200×200 mesh at $t = 0.295$. Fifteen equally spaced contours for density $\rho \in [0.556, 9.170]$ (top left), pressure $p \in [0.010, 0.774]$ (top right), Mach number $|\mathbf{u}|/c \in [0, 2.505]$ (bottom left), and magnetic pressure $|\mathbf{B}|^2/2 \in [0.013, 0.659]$. (bottom right).

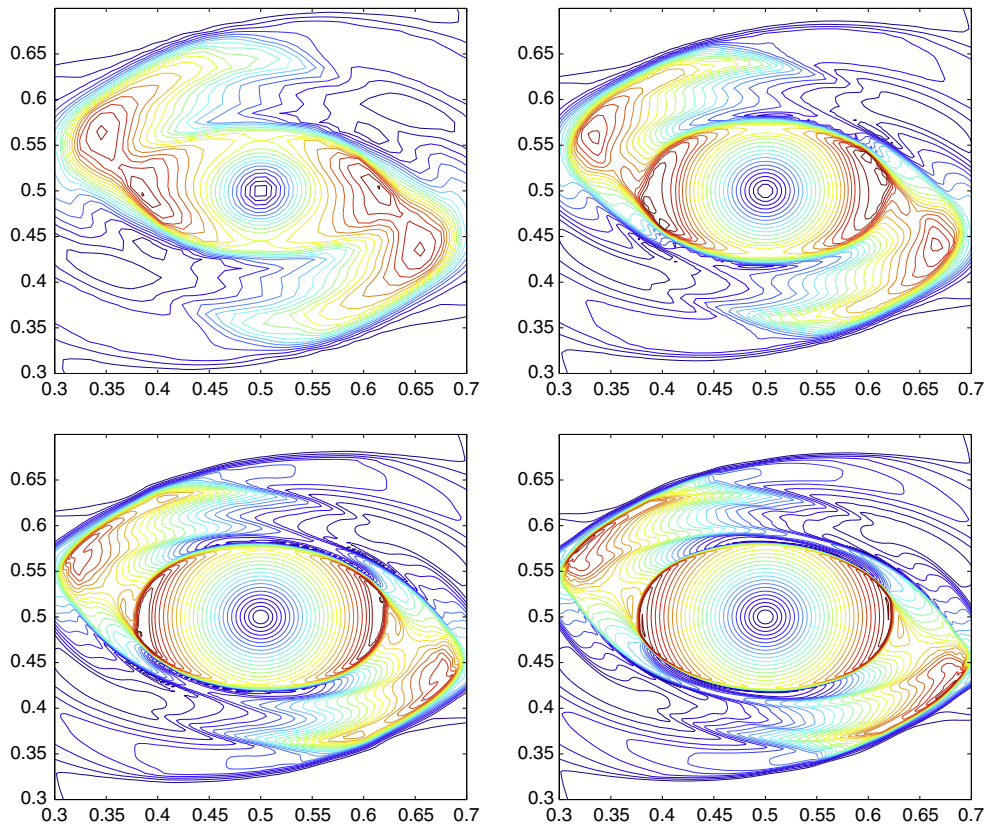


Fig. 6. Zoom-in central part for P^2 approximations of Mach number in the rotor problem at $t = 0.295$. Thirty equally spaces contours with the uniform range $[0.18, 3.12]$. Top left: 100×100 mesh; top right: 200×200 mesh; bottom left: 400×400 mesh; bottom right: 800×800 mesh.

several shocks developed in the solution, the convergence of the method is observed. There is overshoot around the strongest shock when the limiter is not applied. This can be expected and the magnitude of the overshoot is reduced when the mesh is refined. When the default CFL number, $C_{cfl} = 0.6$, is used in the simulation with the limiter, an almost identical plot to the right one in Fig. 8 is obtained.

4.2.4. The Brio–Wu shock-tube problem

In this section, we consider the shock-tube problem which was originally used by Brio and Wu [9] to show the generation of the compound waves in the MHD system. We employ the initial condition

$$(\rho, u_{x'}, u_{y'}, u_z, B_{x'}, B_{y'}, B_z, p) = \begin{cases} (1.000, 0, 0, 0, 0.75, +1, 0, 1.0) & \text{for } x' < 0, \\ (0.125, 0, 0, 0, 0.75, -1, 0, 0.1) & \text{for } x' > 0, \end{cases}$$

where (x', y') is a rotated coordinate with α being the angle from the x -axis to the x' -axis. We solve this problem with $\alpha = 0$ and $\alpha = \pi/32$, which corresponds to a one-dimensional shock-tube problem in an unrotated and a rotated two-dimensional frame, respectively. Outgoing boundary conditions are used with $\gamma = 2$.

For $\alpha = 0$, the simulation is implemented in the domain $[-1, 1] \times [-0.01, 0.01]$ with the 800×8 and 1600×16 meshes, and ρ, B_x, B_y (same as $B_{x'}$ and $B_{y'}$) at $t = 0.2$ with $y = 0$ (same as $y' = 0$) are shown on the left in Fig. 9. The solution of this Riemann problem includes the left moving waves: the fast rarefaction wave, the intermediate shock attached by a slow rarefaction wave; and the right moving waves: the contact discontinuity, a slow shock, and a fast rarefaction wave, and all of them are resolved well. For $\alpha = \pi/32$, the simulation is implemented in the domain $[-1, 1] \times [-1, 1]$ with a 600×600 mesh, and $\rho, B_{x'}, B_{y'}$ at $t = 0.2$ with $y' = 0$ are shown on the right in Fig. 9. Note ρ and $B_{y'}$ in the rotated frame compare well with those in the unrotated one. Oscillation is observed in $B_{x'}$ in the rotated frame, and it does not lead to additional oscillation in the remaining components of the solution. Numerical experiment indicates that the oscillation in $B_{x'}$ is partially due to the initialization procedure, see Fig. 10, where $B_{x'}$ is computed based on the initial numerical solution of B_x and B_y . In the end, we want to comment on the numerical boundary condition. For cases with small α , the error introduced through the non-physical outgoing boundary condition treatment does not have much effect to the solution in the interior of the computational domain at $t = 0.2$. When α is larger, a more robust and accurate boundary condition is needed especially on the domain

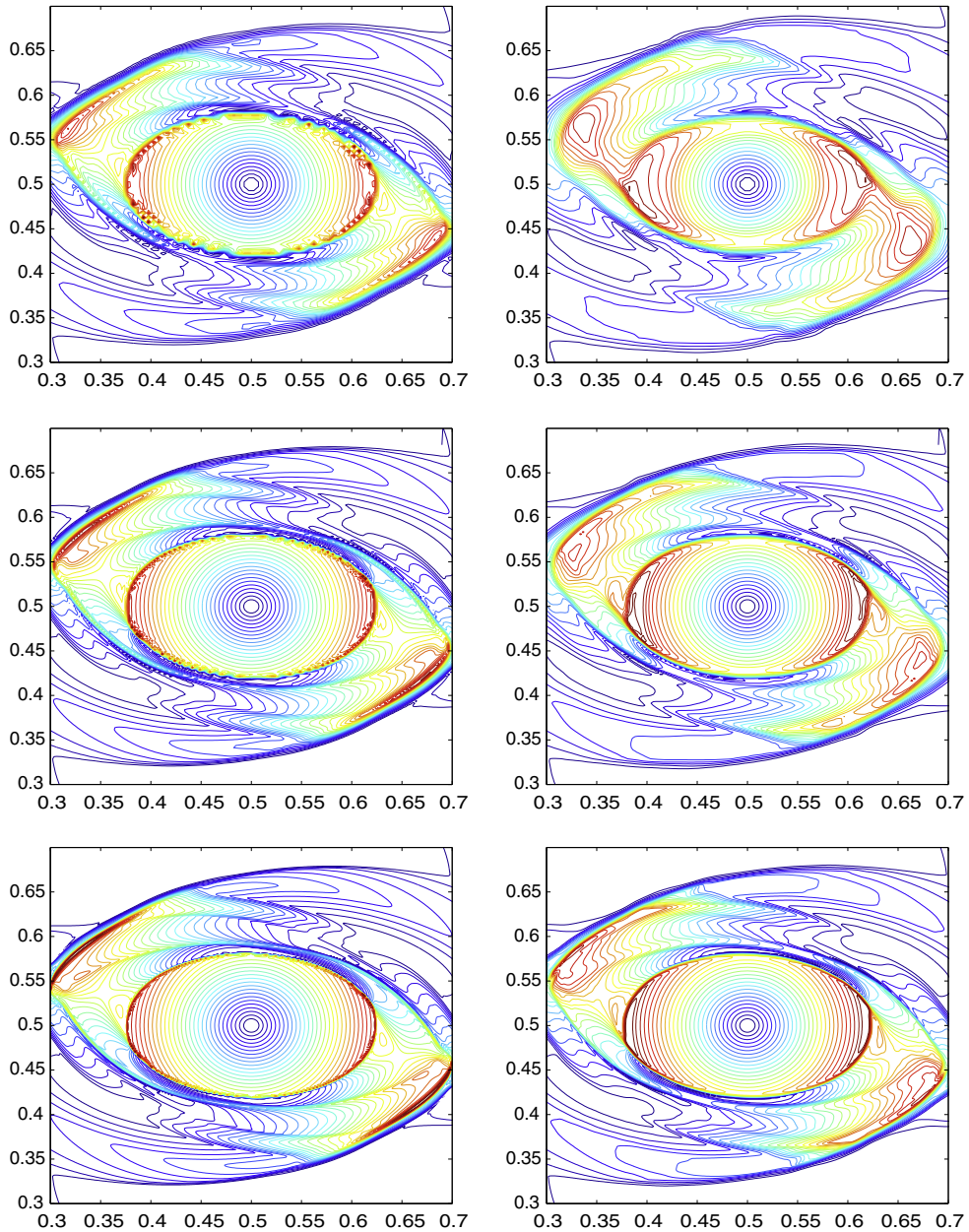


Fig. 7. Zoom-in central part for P^2 approximations of Mach number in the rotor problem at $t = 0.295$. Thirty equally spaced contours with the unique range $[0.18, 3.12]$. From top to bottom: 200×200 mesh, 400×400 mesh, 800×800 mesh. Left: without limiter; right: with limiter.

boundaries which intersect the y' -axis, and this is beyond the scope of this paper. In [31] (see Section 6.3.2), a shifted periodic type boundary condition is used according to the translational symmetry of the problem when the value of α is related to the meshsize. Unfortunately, such strategy cannot be applied to our simulation as it does not preserve the global divergence-free property of the magnetic field.

4.2.5. The blast problem

The blast wave problem was first introduced in [5], and the solution involves strong magnetosonic shocks. We employ the same initial condition as in [5,23], that is $(\rho, u_x, u_y, u_z, B_x, B_y, B_z) = (1, 0, 0, 0, 100/\sqrt{4\pi}, 0, 0)$, and the pressure is given as

$$p = \begin{cases} 1000 & \text{if } r \leq R, \\ 0.1 & \text{if } r > R, \end{cases}$$

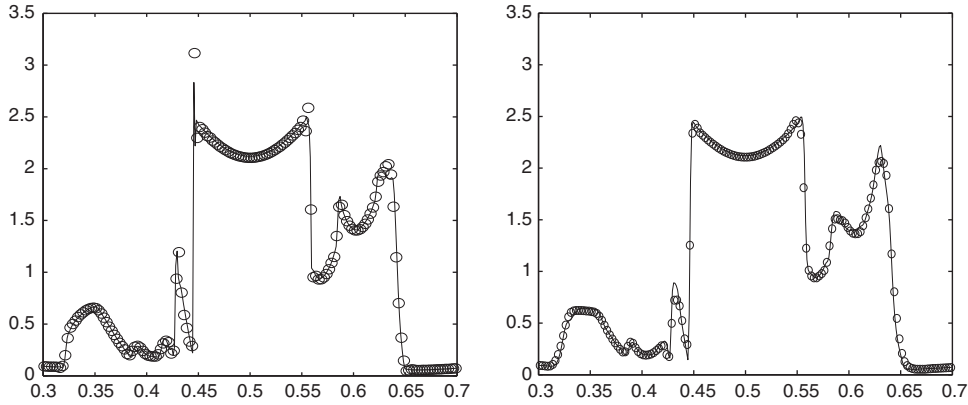


Fig. 8. The Mach number in the rotor problem with $x = 0.413$ at $t = 0.295$. P^2 approximations on the 400×400 mesh (circle) and the 800×800 mesh (solid line). Left: without limiter; right: with limiter.

where $r = \sqrt{x^2 + y^2}$ and $R = 0.1$. With this setup, the fluid in the region outside the initial pressure pulse has a very small plasma $\beta \left(= \frac{p}{(B_x^2 + B_y^2)/2} = 2.513E - 04 \right)$. The simulation is implemented in the domain $[-0.5, 0.5] \times [-0.5, 0.5]$ with the 200×200 mesh. Outgoing boundary conditions are used, and $\gamma = 1.4$.

In Fig. 11, we present the numerical results at $t = 0.01$ based on P^2 approximations, and they are for the density ρ , pressure p , square of the total velocity $u_x^2 + u_y^2$, and the magnetic pressure $B_x^2 + B_y^2$. As pointed out in [5,23], this is a stringent problem to solve. The negative pressure is generated near the shock front during our simulation, and this is also observed by others, e.g. in [23]. One can see in Fig. 12 the images of the pressure p and its negative part $\min(0, p)$ with P^2 approximations. Note that the magnitude of the negative pressure is fairly small for this low plasma β example, and this illustrates the good performance of the proposed methods. (One can recall how the pressure is computed based on other conservative variables).

To further investigate the behavior of the proposed schemes for this example, we plot in Fig. 13 the density ρ , pressure p , $\sqrt{u_x^2 + u_y^2}$, and $\sqrt{B_x^2 + B_y^2}$ at $y = 0$ computed on 200×200 and 400×400 meshes. One can see the scheme performs well in convergence, and the negative pressure appears mainly around the shock front. For this example, all reported results are obtained when the componentwise TVB minmod limiter is applied. And the simulations with limiters implemented in the local characteristic fields suffer from the pressure being negative in terms of stability. It is expected that positivity preserving techniques will further enhance the numerical stability, and this will be left to our future investigation.

4.2.6. The cloud-shock interaction

The last example we consider is the cloud-shock interaction problem [14] which involves strong MHD shocks interacting with a dense cloud. We define three sets of data for $(\rho, u_x, u_y, u_z, B_x, B_y, B_z, p)$ as

$$\begin{aligned} \mathbf{U}_1 &= (3.88968, 0, 0, -0.05234, 1, 0, 3.9353, 14.2614), \\ \mathbf{U}_2 &= (1, -3.3156, 0, 0, 1, 0, 1, 0.04), \quad \mathbf{U}_3 = (5, -3.3156, 0, 0, 1, 0, 1, 0.04). \end{aligned}$$

The computational domain $[0, 2] \times [0, 1]$ is divided into three regions: the post-shock region $\Omega_1 = \{(x, y) : 0 \leq x \leq 1.2, 0 \leq y \leq 1\}$, the pre-shock region $\Omega_2 = \left\{ (x, y) : 1.2 < x \leq 2, 0 \leq y \leq 1, \sqrt{(x - 1.4)^2 + (y - 0.5)^2} \geq 0.18 \right\}$, and the cloud region $\Omega_3 = \left\{ (x, y) : \sqrt{(x - 1.4)^2 + (y - 0.5)^2} < 0.18 \right\}$. The solutions in Ω_1, Ω_2 and Ω_3 are initialized as $\mathbf{U}_1, \mathbf{U}_2$, and \mathbf{U}_3 , respectively. Note that the cloud taking up the region Ω_3 is five times denser than its surrounding. Outgoing boundary conditions are used, and $\gamma = 5/3$.

Fig. 14 shows the gray-scale images (with the darker area representing the larger value) on the mesh 600×300 for the P^2 approximations of the density ρ , the magnetic field component B_x and B_y , and the pressure p at $t = 0.6$. With the main features comparable to those in [14], our results also show some difference. For example, two middle tails of the cloud in [14] seem to bend much further towards $y = 0.5$. To gain confidence in our results, we further perform a convergence study through the P^2 approximations on 600×300 and 800×400 meshes at $t = 0.6$. And the cuts of the density at $y = 0.6$ and at $x = 1.0$ are plotted in Fig. 15. The convergence of our scheme is confirmed, and in particular, the thickness of the cloud along the y direction at $x = 1.0$ is consistently captured on both meshes. The reported results are obtained by applying the limiter in local characteristic fields.

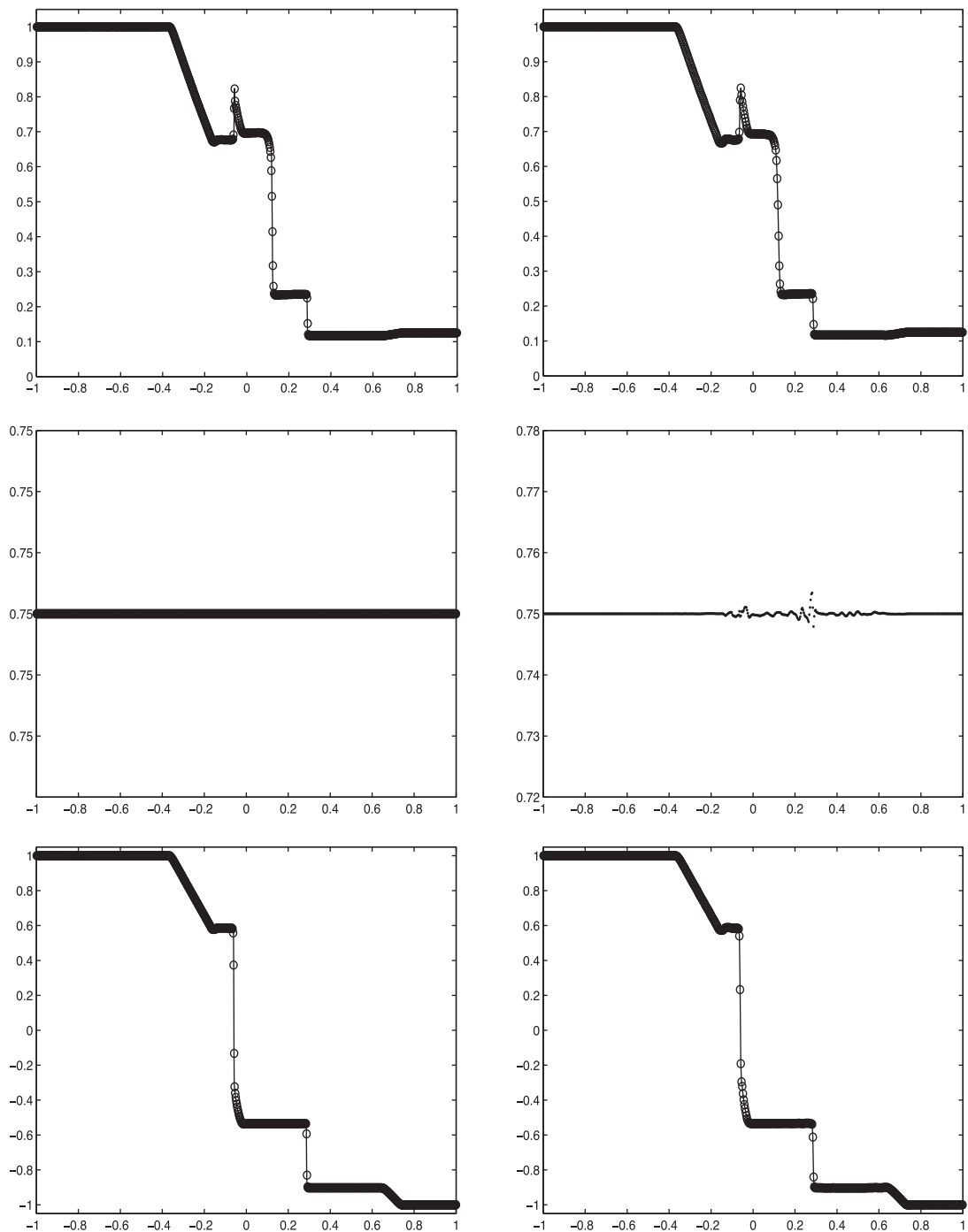


Fig. 9. P^2 approximations for the shock-tube problem in a rotated coordinate (x',y') with α being the angle from the x -axis to the x' -axis. From top to bottom: ρ , B_x , B_y at $t = 0.2$ with $y = 0$. Left: 800×8 mesh (circle) and 1600×16 mesh (solid line) on $[-1,1] \times [-0.01,0.01]$ with $\alpha = 0$; right: 600×600 mesh on $[-1,1] \times [-1,1]$ with $\alpha = \pi/32$.

4.3. Remarks on the computational cost

In the end, we want to briefly comment on the computational cost of the proposed schemes. On one hand, the methods do not use approximate or exact Riemann solvers, and they allow larger time steps compared with schemes such as standard DG methods ([27]), these properties will contribute to the reduction of the computational cost. On the other hand, the use of two

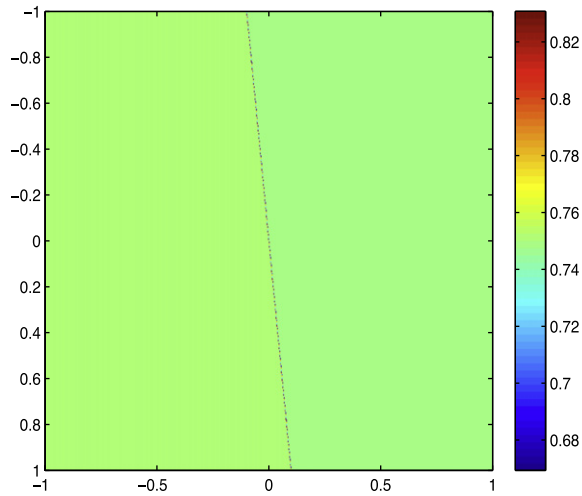


Fig. 10. The P^2 initialization of B_x for the shock-tube problem in a rotated coordinate (x', y') with $\alpha = \pi/32$ being the angle from the x -axis and the x' -axis.

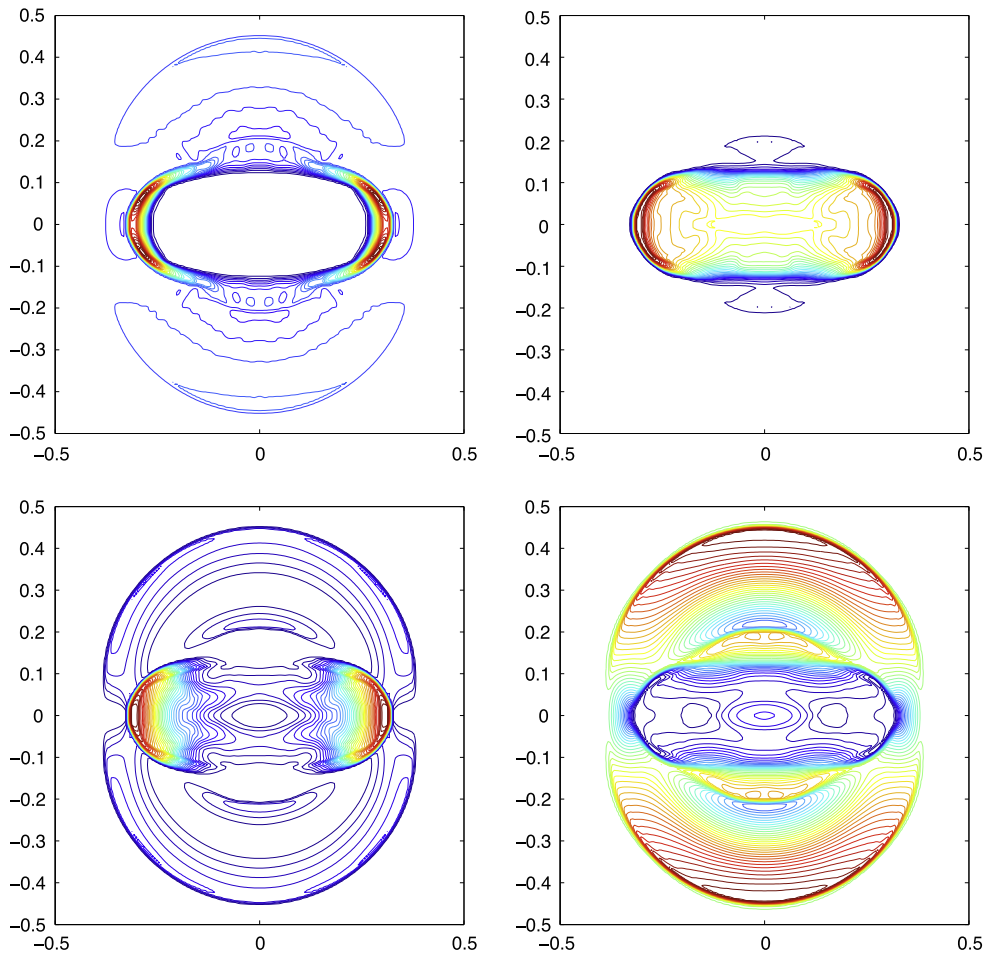


Fig. 11. P^2 approximations for the blast problem on the 200×200 mesh at $t = 0.01$. Forty equally spaced contours are used. Top left: density $\rho \in [0.206, 4.751]$; top right: pressure $p \in [-1.633, 258.418]$; bottom left: square of total velocity $u_x^2 + u_y^2 \in [0, 286.125]$; bottom right: magnetic pressure $B_x^2 + B_y^2 \in [430.091, 1183.430]$.

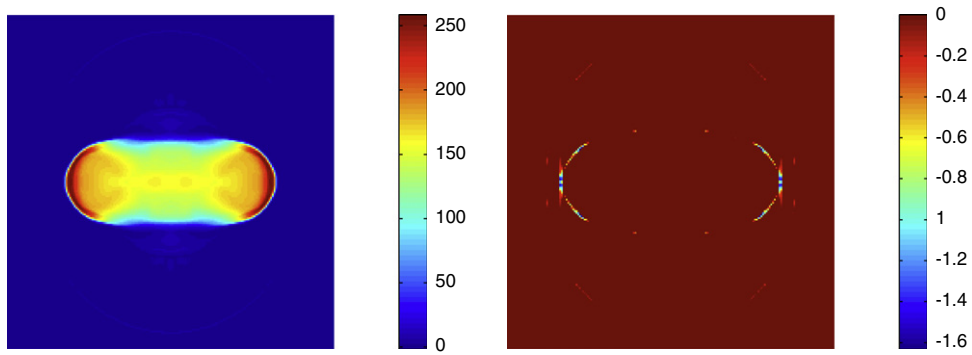


Fig. 12. P^2 approximation of the pressure in the blast problem on the 200×200 mesh at $t = 0.01$. Left: pressure p ; right: $\min(0, p)$.

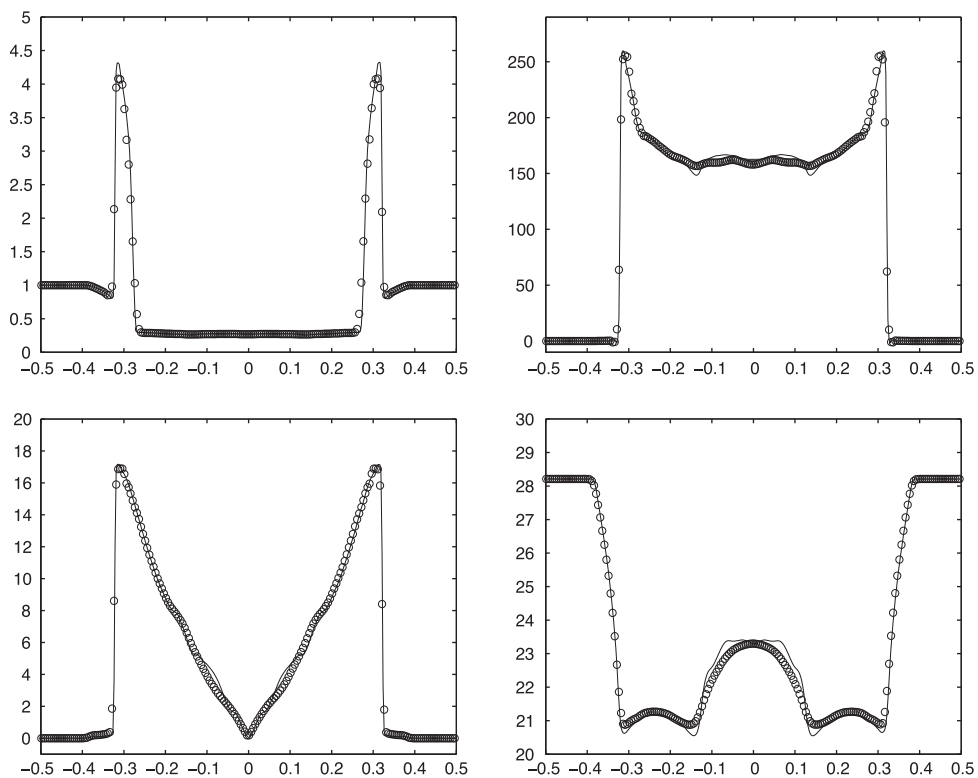


Fig. 13. P^2 approximations for the blast problem with $y = 0$ at $t = 0.01$. The density ρ (top left), pressure p (top right), $\sqrt{u_x^2 + u_y^2}$ (bottom left), and $\sqrt{B_x^2 + B_y^2}$ (bottom right) on the 200×200 mesh (circle) and the 400×400 mesh (solid line).

copies of numerical solutions and the divergence-free reconstruction step will increase the computational complexity. As some reference, we report the CPU time in Table 5 to run 100 time steps of the proposed methods. The simulation is performed on a computer with the 2.53 GHz Intel Core 2 Duo processor and 4 GB DDR3 memory. One can observe that to run one time step of the P^2 simulation on the $N \times N$ mesh, the cost is comparable to that of the P^1 simulation on the $2N \times 2N$ mesh, and it is almost 4 times of the cost to run one time step of the P^1 simulation on the $N \times N$ mesh.

5. Concluding remarks

In this paper, the second and the third order central DG methods are proposed for ideal MHD equations in two dimensions when the Cartesian meshes are used. With the exactly divergence-free magnetic field, the methods demonstrate good stability with designed accuracy. In the ongoing and future projects, we will extend the methods to higher order accuracy, three

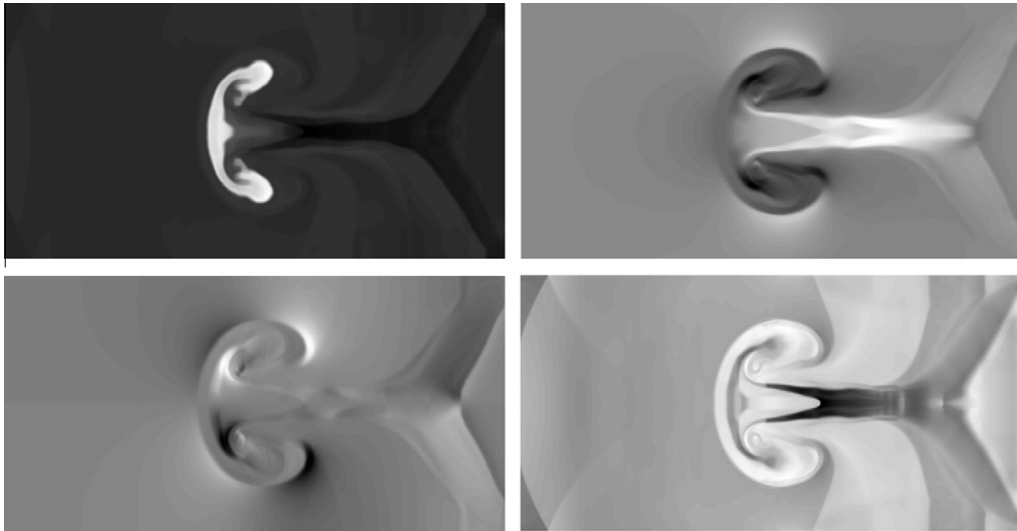


Fig. 14. Gray-scaled images for P^2 approximations of the cloud-shock interaction problem on the 600×300 mesh at $t = 0.6$. Top left: $\rho \in [1.856, 11.269]$; top right: $B_x \in [-2.722, 4.179]$; bottom left: $B_y \in [-2.913, 2.913]$; bottom right: $p \in [6.541, 14.675]$.

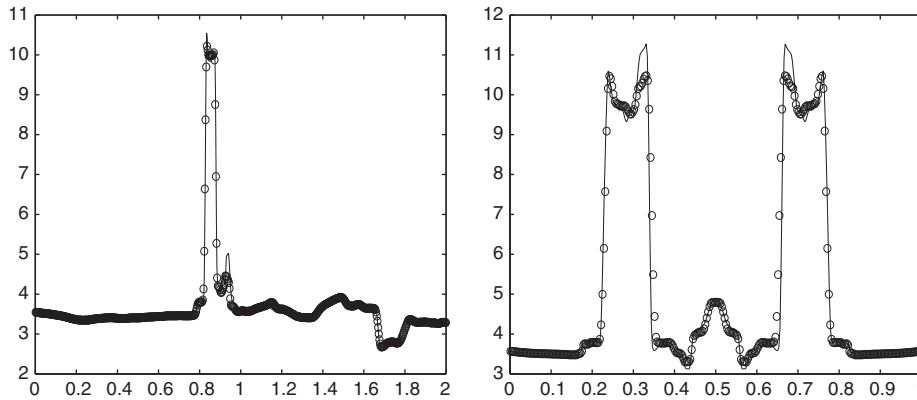


Fig. 15. The P^2 approximations of ρ in the cloud-shock interaction problem on the 600×300 mesh (circle) and the 800×400 (solid line) at $t = 0.6$. Left: $y = 0.6$; right: $x = 1.0$.

Table 5

The CPU time (in seconds) to run 100 time steps of the proposed methods for the smooth Alfvén wave example.

Mesh	32×32	64×64	128×128	256×256
p^1	3.015	13.535	60.099	255.599
p^2	12.523	56.890	232.927	926.234

dimensions, and hopefully also to general meshes. Moreover, positivity preserving techniques will be explored in central DG framework to further improve the stability of the algorithms.

Acknowledgments

This research is partially supported by NSF Grant DMS-0652481, DMS-0636358 (RTG), NSF CAREER award DMS-0847241, and an Alfred P. Sloan Research Fellowship.

Appendix A. Formulas for divergence-free reconstructions

In this section, we include the explicit formulas of divergence-free reconstructions used in Section 3.2.2. A reference element $C = (-1, 1) \times (-1, 1)$ is considered for simplicity, and formulas for general elements can be obtained through change of variables.

Given $b_x^-(y), b_x^+(y), b_y^-(x), b_y^+(x) \in P^k(\mathbb{R})$, satisfying the compatibility condition

$$\int_{-1}^1 b_x^+(y) dy - \int_{-1}^1 b_x^-(y) dy + \int_{-1}^1 b_y^+(x) dx - \int_{-1}^1 b_y^-(x) dx = 0. \quad (\text{A.1})$$

The divergence-free reconstruction is to look for $\mathcal{B} = (B_x, B_y)^\top \in \mathcal{W}^k(C)$, such that

$$B_x(\pm 1, y) = b_x^\pm(y), \quad B_y(x, \pm 1) = b_y^\pm(x), \quad \text{and} \quad \nabla \cdot \mathcal{B} = 0.$$

This reconstruction is uniquely determined for $k = 1$ and $k = 2$, and they are second and third order accurate, respectively. The compatibility condition (A.1) is corresponding to (17).

When $k = 1$, given

$$b_x^\pm(y) = a_0^\pm + a_1^\pm y, \quad b_y^\pm(x) = b_0^\pm + b_1^\pm x$$

with the compatibility condition (A.1) being $a_0^+ - a_0^- + b_0^+ - b_0^- = 0$, the reconstructed divergence-free magnetic field $\mathcal{B} = (B_x, B_y) \in \mathcal{W}^1(C)$ is uniquely determined as

$$\begin{aligned} B_x(x, y) &= a_0 + a_1 x + a_2 y + a_3 x^2 + a_4 xy, \\ B_y(x, y) &= b_0 + b_1 x + b_2 y + b_3 xy + b_4 y^2 \end{aligned}$$

with

$$\begin{aligned} a_1 &= \frac{1}{2}(a_0^+ - a_0^-), & b_1 &= \frac{1}{2}(b_1^+ + b_1^-), \\ a_2 &= \frac{1}{2}(a_1^+ + a_1^-), & b_2 &= \frac{1}{2}(b_0^+ - b_0^-), \\ a_4 &= -2b_4 = \frac{1}{2}(a_1^+ - a_1^-), & b_0 &= \frac{1}{2}(b_0^+ + b_0^-) - b_4, \\ b_3 &= -2a_3 = \frac{1}{2}(b_1^+ - b_1^-), & a_0 &= \frac{1}{2}(a_0^+ + a_0^-) - a_3. \end{aligned}$$

When $k = 2$, given

$$b_x^\pm(y) = a_0^\pm + a_1^\pm y + a_2^\pm y^2, \quad b_y^\pm(x) = b_0^\pm + b_1^\pm x + b_2^\pm x^2$$

with the compatibility condition (A.1) being

$$a_0^+ - a_0^- + \frac{1}{3}(a_2^+ - a_2^-) + b_0^+ - b_0^- + \frac{1}{3}(b_2^+ - b_2^-) = 0,$$

the reconstructed divergence-free magnetic field $\mathcal{B} = (B_x, B_y) \in \mathcal{W}^2(C)$ is uniquely determined as

$$\begin{aligned} B_x(x, y) &= a_0 + a_1 x + a_2 y + a_3 x^2 + a_4 xy + a_5 y^2 + a_6 x^3 + a_7 xy^2, \\ B_y(x, y) &= b_0 + b_1 x + b_2 y + b_3 x^2 + b_4 xy + b_5 y^2 + b_6 x^2 y + b_7 y^3 \end{aligned}$$

with

$$\begin{aligned} b_1 &= \frac{1}{2}(b_1^+ + b_1^-), & a_2 &= \frac{1}{2}(a_1^+ + a_1^-), \\ b_4 &= -2a_3 = \frac{1}{2}(b_1^+ - b_1^-), & b_3 &= \frac{1}{2}(b_2^+ + b_2^-), \\ a_4 &= -2b_5 = \frac{1}{2}(a_1^+ - a_1^-), & a_5 &= \frac{1}{2}(a_2^+ + a_2^-), \\ a_7 &= -3b_7 = \frac{1}{2}(a_2^+ - a_2^-), & a_0 &= \frac{1}{2}(a_0^+ + a_0^-) - a_3, \\ b_6 &= -3a_6 = \frac{1}{2}(b_2^+ - b_2^-), & b_0 &= \frac{1}{2}(b_0^+ + b_0^-) - b_5, \\ a_1 &= -b_2 = \frac{1}{2}(a_0^+ - a_0^-) - a_6. \end{aligned}$$

References

- [1] J. Balbas, E. Tadmor, C.-C. Wu, Non-oscillatory central schemes for one- and two-dimensional MHD equations, *Journal of Computational Physics* 201 (2004) 261–285.
- [2] D.S. Balsara, Divergence-free adaptive mesh refinement for magnetohydrodynamics, *Journal of Computational Physics* 174 (2001) 614–648.
- [3] D.S. Balsara, Second order accurate schemes for magnetohydrodynamics with divergence-free reconstruction, *Astrophysical Journal Supplement Series* 151 (2004) 149–184.

- [4] D.S. Balsara, Divergence-free reconstruction of magnetic fields and WENO schemes for magnetohydrodynamics, *Journal of Computational Physics* 228 (2009) 5040–5056.
- [5] D.S. Balsara, D.S. Spicer, A staggered mesh algorithm using high order Godunov fluxes to ensure solenoidal magnetic fields in magnetohydrodynamic simulations, *Journal of Computational Physics* 149 (1999) 270–292.
- [6] T. Barth, On the role of involutions in the discontinuous Galerkin discretization of Maxwell and magnetohydrodynamic systems, in: Arnold, Bochev, Shashkov (Eds.), *Compatible Spatial Discretizations, IMA Volumes in Mathematics and its Applications*, vol. 142, 2006, pp. 69–88.
- [7] J.U. Brackbill, D.C. Barnes, The effect of nonzero $\nabla \cdot \mathbf{B}$ on the numerical solution of the magnetohydrodynamic equations, *Journal of Computational Physics* 35 (1980) 426–430.
- [8] F. Brezzi, J. Douglas Jr., L.D. Marini, Two families of mixed finite elements for second order elliptic problems, *Numerische Mathematik* 47 (1985) 217–235.
- [9] M. Brio, C.-C. Wu, An upwind differencing scheme for the equations of ideal magnetohydrodynamics, *Journal of Computational Physics* 75 (1988) 400–422.
- [10] B. Cockburn, F. Li, C.-W. Shu, Locally divergence-free discontinuous Galerkin methods for the Maxwell equations, *Journal of Computational Physics* 194 (2004) 588–610.
- [11] B. Cockburn, C.-W. Shu, Runge–Kutta discontinuous Galerkin methods for convection-dominated problems, *Journal of Scientific Computing* 16 (2001) 173–261.
- [12] B. Cockburn, C.-W. Shu, The Runge–Kutta discontinuous Galerkin method for conservation laws V: multidimensional systems, *Journal of Computational Physics* 141 (1998) 199–224.
- [13] W. Dai, P.R. Woodward, An approximate Riemann solver for ideal magnetohydrodynamics, *Journal of Computational Physics* 111 (1994) 354–372.
- [14] W. Dai, P.R. Woodward, Extension of the piecewise parabolic method to multidimensional ideal magnetohydrodynamics, *Journal of Computational Physics* 115 (1994) 485–514.
- [15] A. Dedner, F. Kemm, D. Kröner, C.-D. Munz, T. Schnitner, M. Wesenberg, Hyperbolic divergence cleaning for the MHD equations, *Journal of Computational Physics* 175 (2002) 645–673.
- [16] C.R. Evans, J.F. Hawley, Simulation of magnetohydrodynamic flows: a constrained transport method, *Astrophysical Journal* 332 (1988) 659–677.
- [17] T.A. Gardiner, J.M. Stone, An unsplit Godunov method for ideal MHD via constrained transport, *Journal of Computational Physics* 205 (2005) 509–539.
- [18] S.K. Godunov, Symmetric form of the equations of magnetohydrodynamics, *Numerical Methods for Mechanics of Continuum Medium* 1 (1972) 26–34.
- [19] S. Gottlieb, C.-W. Shu, E. Tadmor, Strong stability preserving high order time discretization methods, *SIAM Review* 43 (2001) 89–112.
- [20] R.J. Leveque, *Finite Volume Methods for Hyperbolic Problems*, Cambridge University Press, 2002.
- [21] F. Li, C.-W. Shu, Locally divergence-free discontinuous Galerkin methods for MHD equations, *Journal of Scientific Computing* 22 (2005) 413–442.
- [22] S. Li, An HLLC Riemann solver for magneto-hydrodynamics, *Journal of Computational Physics* 203 (2005) 344–357.
- [23] S. Li, High order central scheme on overlapping cells for magneto-hydrodynamic flows with and without constrained transport method, *Journal of Computational Physics* 227 (2008) 7368–7393.
- [24] S. Li, A fourth-order divergence-free method for MHD flows, *Journal of Computational Physics* 229 (2010) 7893–7910.
- [25] Y. Liu, C.-W. Shu, E. Tadmor, M. Zhang, Non-oscillatory hierarchical reconstruction for central and finite-volume schemes, *Communications in Computational Physics* 2 (2007) 933–963.
- [26] Y. Liu, C.-W. Shu, E. Tadmor, M. Zhang, Central discontinuous Galerkin methods on overlapping cells with a nonoscillatory hierarchical reconstruction, *SIAM Journal on Numerical Analysis* 45 (2007) 2442–2467.
- [27] Y. Liu, C.-W. Shu, E. Tadmor, M. Zhang, L^2 stability analysis of the central discontinuous Galerkin method and a comparison between the central and regular discontinuous Galerkin methods, *ESAIM: Mathematical Modelling and Numerical Analysis* 42 (2008) 593–607.
- [28] K.G. Powell, An approximate Riemann solver for magnetohydrodynamics (that works in more than one dimension), ICASE Report No. 94-24, Langley, VA, 1994.
- [29] J. Qiu, C.-W. Shu, Runge–Kutta discontinuous Galerkin method using WENO limiters, *SIAM Journal on Scientific Computing* 26 (2005) 907–929.
- [30] C.-W. Shu, TVB uniformly high-order schemes for conservation laws, *Mathematics of Computation* 49 (1987) 105–121.
- [31] G. Tóth, The $\nabla \cdot \mathbf{B} = 0$ constraint in shock-capturing magnetohydrodynamics codes, *Journal of Computational Physics* 161 (2000) 605–652.